

Flux-normalized wavefield decomposition and migration of seismic data

Bjørn Ursin* and Ørjan Pedersen* and Børge Arntsen**

ABSTRACT

Separation of wavefields into directional components can be accomplished by an eigenvalue decomposition of the accompanying system matrix. In conventional pressure-normalized wavefield decomposition, the resulting directional decomposed differential equations contain an interaction between directional components, and depend on the reflectivity function. Usually, the interaction between directional components is disregarded, and by accounting for the reflectivity function, amplitude information is improved. By directional wavefield decomposition using flux-normalized eigenvalue decomposition, it is possible to simplify the resulting system differential equations. Disregarding directional component interaction in the flux-normalized approach provides wavefield separation independent on reflectivity function, and amplitude information is preserved. As a result, reflectivity images with improved amplitude information can be beneficial as indicators of hydrocarbon or in wave-equation migration velocity analysis.

computationally cheap and robust alternative approach for solving the wave-equation. With wavefield propagators based on one-way methods, one can increase the speed of computations by several orders of magnitude compared to full wavefield methods.

Representation of a wavefield using the one-way wave-equation permits separation of the wavefield into up- and downgoing constituents. This separation is not valid for near-horizontal propagating waves. Schemes for splitting the wave-equation into up- and downgoing parts and seismic mapping of reflectors are discussed by Claerbout (1971, 1970); however, only the traveltimes are handled correctly.

Several authors have investigated various methods for amplitude correction to one-way wave-equations. Zhang et al. (2003, 2005, 2007) addresses true-amplitude implementation of one-way wave-equations in common-shot migration by modifying the one-way wave-equation. This is accomplished by introducing an auxiliary function that corrects the leading order transport equation for the full wave-equation. Ray theory applied to the modified one-way equations yield up- and downgoing eikonal equations with amplitudes satisfying the transport equation. With full wave-form solutions substituted with corresponding ray-theoretical approximations provides true-amplitude in the sense that the imaging formulas reduce to a Kirchhoff common-shot inversion expression.

Kiyashchenko et al. (2005) develop improved estimation of amplitudes using a multi-one-way approach. It is developed from an iterative solution of the factorized two-way wave-equation with a right-hand side incorporating the medium heterogeneities. It allows for both vertical and horizontal velocity variations and it is demonstrated that the multi-one-way scheme reduce errors in amplitude estimates compared to conventional one-way propagators.

Cao and Wu (2008) reformulate the solution of the one-way wave-equation in smoothly varying one-dimensional media based on energy-flux conservations. By introducing transparent boundary conditions and transparent propagators, their formulation is extended to a general hetero-

INTRODUCTION

Accurate wavefield traveltimes and amplitudes can be described using two-way wave-equation techniques like finite-difference or finite-element methods. However, these methods can often be significantly more computationally expensive compared to one-way methods. The computational cost in modelling wavefield extrapolation using full wave-equation methods can become a limitation for three-dimensional applications in particular. Ray methods based upon asymptotic theory provide effective alternatives to full wave-equation methods; however, their high-frequency approximations restrict their use in complex subsurface geometry. One-way wavefield methods based upon a paraxial approximation of the wave-equation provide a both

geneous media in the local angle domain utilizing beamlet methods.

By decomposing the wavefield into up- and downgoing waves with an eigenvalue decomposition using symmetry properties of the accompanying system matrix, one can derive simplified equations for computing the wavefield propagators. This directional decomposition is consistent with a flux-normalization of the wavefield (Ursin, 1983). Further, by neglecting coupling terms between the up- and downgoing waves, the resulting system matrix can be used as a starting point to derive paraxial approximations of the original wave-equation. They can also be used to derive WKBJ approximations of various orders (Bremmer, 1951; van Stralen et al., 1998).

In this paper, we derive initial conditions and one-way propagators for flux-normalized wavefield extrapolation in 1D media and show how this provides accurate amplitude information. We formulate an unbiased estimate of the reflectivity using the wave-equation angle transform. Further, we propose an extension to a general heterogeneous media by defining a laterally invariant background media in which the flux-normalization and an approximation to the transmission loss is performed. We account for the medium perturbations in the downward propagation using Fourier finite-difference methods (Ristow and Rühl, 1994).

We apply both conventional pressure-normalized and the derived flux-normalized wavefield decomposition and propagation to a field data example from offshore Norway. Using this example, we compare and quantify the estimated reflectivity differences.

LATERALLY HOMOGENEOUS MEDIUM

We consider acoustic waves travelling in a three-dimensional medium where the principal direction of propagation is taken along the x_3 axis (or “depth”), and the transverse axes are (x_1, x_2) . The acoustic medium parameters are assumed to be functions of depth x_3 only. Let c denote the propagation velocity; $\mathbf{v} = (v_1, v_2, v_3)$ the displacement velocity vector; p the pressure; and ρ the density of the medium. With no external volume force acting on the medium, the acoustic wavefield satisfies the constitutive relation given by (Pierce, 1981) (equation 1-5.3)

$$-\nabla p = \rho \partial_t \mathbf{v}, \quad (1)$$

and the equation of motion given by

$$\frac{1}{c^2} \partial_t p + \rho \nabla \cdot \mathbf{v} = 0, \quad (2)$$

where $\nabla = (\partial_1, \partial_2, \partial_3)$ and ∂_t denotes the partial derivative with respect to time t .

We define the Fourier transform with respect to time t and the transverse spatial directions (x_1, x_2) as

$$P(\omega, k_1, k_2, x_3) = \iiint_{-\infty}^{\infty} p(t, x_1, x_2, x_3) e^{i(\omega t - k_1 x_1 - k_2 x_2)} dx_1 dx_2 dt, \quad (3)$$

with the inverse transform with respect to circular frequency ω and the transverse wave-numbers (k_1, k_2) as

$$p(t, x_1, x_2, x_3) = \frac{1}{(2\pi)^3} \iiint_{-\infty}^{\infty} P(\omega, k_1, k_2, x_3) e^{i(-\omega t + k_1 x_1 + k_2 x_2)} dk_1 dk_2 d\omega. \quad (4)$$

Applying the Fourier transform to equations 1 and 2, the resulting reduced linear acoustic system of equations in a horizontally homogeneous fluid yield the matrix differential equation

$$\partial_3 \mathbf{b} = i\omega \mathbf{A} \mathbf{b}, \quad (5)$$

where the system matrix \mathbf{A} is given by

$$\mathbf{A} = \begin{bmatrix} 0 & \rho \\ \frac{1}{\rho} \left(\frac{1}{c^2} - \frac{k_1^2 + k_2^2}{\omega^2} \right) & 0 \end{bmatrix}, \quad (6)$$

and the field vector \mathbf{b} by

$$\mathbf{b} = \begin{bmatrix} P \\ V_3 \end{bmatrix}, \quad (7)$$

where P is the Fourier transformation of p and V_3 is the Fourier transformation of v_3 with respect to t , x_1 and x_2 .

The measured field vector $\mathbf{b} = [P, V_3]^T$ can be separated into up- and downgoing waves, denoted U and D , respectively. This separation is accomplished by applying an inverse eigenvector matrix of \mathbf{A} , denoted \mathbf{L}^{-1} , on \mathbf{b} . We define the transformed field vector containing the directional decomposed wavefield by

$$\mathbf{w} = \begin{bmatrix} U \\ D \end{bmatrix} = \mathbf{L}^{-1} \mathbf{b}. \quad (8)$$

Moreover, upon substitution of \mathbf{w} , the matrix differential equation 5 transforms to

$$\partial_3 \mathbf{w} = (i\omega \mathbf{\Lambda} - \mathbf{L}^{-1} \partial_3 \mathbf{L}) \mathbf{w}, \quad (9)$$

where an eigenvalue decomposition of \mathbf{A} provides the diagonal eigenvalue matrix $\mathbf{\Lambda} = \mathbf{L}^{-1} \mathbf{A} \mathbf{L}$.

The vertical wave-number k_3 is

$$k_3 = \begin{cases} \sqrt{\left(\frac{\omega}{c}\right)^2 - (k_1^2 + k_2^2)}, & \text{if } \sqrt{k_1^2 + k_2^2} \leq \left|\frac{\omega}{c}\right| \\ i\sqrt{k_1^2 + k_2^2 - \left(\frac{\omega}{c}\right)^2}, & \text{if } \sqrt{k_1^2 + k_2^2} > \left|\frac{\omega}{c}\right| \end{cases}. \quad (10)$$

We consider a plane wave with wavenumber $\mathbf{k} = (k_1, k_2, k_3)^T$ and direction $\mathbf{m} = (\sin \theta \cos \phi, \sin \theta \sin \phi, \cos \theta)^T$ where θ is dip angle and ϕ is azimuth. We have

$$\mathbf{k} = \frac{\mathbf{m}\omega}{c} = \omega \mathbf{p}, \quad (11)$$

where \mathbf{p} is the slowness vector. In our further development, it is convenient to introduce the impedance Z :

$$Z = \frac{\rho\omega}{k_3} = \frac{\rho}{p_3} = \frac{\rho c}{\cos \theta}. \quad (12)$$

Amplitude-normalized wavefields

In the conventional pressure-normalized wavefield separation approach, one choose the eigenvector matrix of \mathbf{A} as (Claerbout, 1976; Ursin, 1984, 1987)

$$\mathbf{L} = \begin{bmatrix} 1 & 1 \\ -\frac{1}{Z} & \frac{1}{Z} \end{bmatrix}. \quad (13)$$

This leads to the inverse eigenvector matrix

$$\mathbf{L}^{-1} = \frac{1}{2} \begin{bmatrix} 1 & -Z \\ 1 & Z \end{bmatrix}. \quad (14)$$

With the eigenvector matrix defined in equation 13, the matrix differential equation 9 becomes

$$\partial_3 \mathbf{w} = i\omega \begin{bmatrix} -p_3 & 0 \\ 0 & p_3 \end{bmatrix} \mathbf{w} - \gamma(x_3) \begin{bmatrix} -1 & 1 \\ 1 & -1 \end{bmatrix} \mathbf{w}, \quad (15)$$

where

$$\gamma(x_3) = \frac{1}{2} \partial_3 \log Z(x_3) \quad (16)$$

is the reflectivity function. Using equation 12 it can be expressed as

$$\gamma(x_3) = \frac{1}{2} \left[\frac{1}{\rho} \frac{\partial \rho}{\partial x_3} + \frac{1}{\cos^2 \theta} \frac{1}{c} \frac{\partial c}{\partial x_3} \right]. \quad (17)$$

The wavefield decomposition described in equation 15 is referred to as being pressure-normalized in the sense that the pressure field equals the sum of the up- and downgoing wavefield.

We consider a stack of inhomogeneous layers where ρ and c are continuous functions of x_3 within each layer. At an interface between two layers, the boundary condition requires that the wave vector \mathbf{b} shall be continuous. For an interface at $x_3 = x_{3k}$ we must have $L_+ \mathbf{w}_+ = L_- \mathbf{w}_-$ where $L_- = L(x_{3k-})$ is evaluated above the interface, and $L_+ = L(x_{3k+})$ is evaluated beneath the interface (the x_3 -axis is pointing vertically downwards). We therefore have

$$\mathbf{w}_+ = L_+^{-1} L_- \mathbf{w}_-. \quad (18)$$

Equation 13 and 14 give

$$L_+^{-1} L_- = \frac{1}{2} \begin{bmatrix} 1 + \frac{Z_+}{Z_-} & 1 - \frac{Z_+}{Z_-} \\ 1 - \frac{Z_+}{Z_-} & 1 + \frac{Z_+}{Z_-} \end{bmatrix}. \quad (19)$$

This can be written as (Ursin, 1983, equation 33):

$$L_+^{-1} L_- = \frac{1}{2} \begin{bmatrix} T_u^{-1} & R_u T_u^{-1} \\ R_u T_u^{-1} & T_u^{-1} \end{bmatrix}, \quad (20)$$

where T_u and R_u are the transmission and reflection coefficients for an upward travelling incident wave at the interface.

Flux-normalized wavefields

We now derive an alternative directional decomposition by a flux-normalization of the wavefield. The main advantage of flux-normalizing the wavefield is that we obtain simpler expression of the corresponding directional

decomposed matrix differential equation, as compared to the pressure-normalized approach. Disregarding the interaction between directional components yields a matrix differential equation independent of the reflectivity function.

In order obtain a flux-normalized system of equations, we choose the eigenvector matrix of \mathbf{A} as (Ursin, 1983; Wapenaar, 1998)

$$\tilde{\mathbf{L}} = \frac{1}{\sqrt{2}} \begin{bmatrix} \sqrt{Z} & \sqrt{Z} \\ -\frac{1}{\sqrt{Z}} & \frac{1}{\sqrt{Z}} \end{bmatrix}, \quad (21)$$

and thus the inverse eigenvector matrix becomes

$$\tilde{\mathbf{L}}^{-1} = \frac{1}{\sqrt{2}} \begin{bmatrix} \frac{1}{\sqrt{Z}} & -\sqrt{Z} \\ \frac{1}{\sqrt{Z}} & \sqrt{Z} \end{bmatrix}. \quad (22)$$

This provides a flux-normalized representation of the wavefield

$$\tilde{\mathbf{w}} = \tilde{\mathbf{L}}^{-1} \mathbf{b}, \quad (23)$$

where $\tilde{\mathbf{w}} = (\tilde{U}, \tilde{D})^T$, and where \tilde{U} and \tilde{D} denote the flux-normalized directional components of the wavefield. The wavefield is referred to as flux-normalized in the sense that the energy flux in the x_3 -direction is propagation invariant (Ursin, 1983; Wapenaar, 1998).

Both the pressure-normalized and the flux-normalized decomposition break down for near horizontally travelling waves since the lateral wave-number k_3 approaches 0 in the horizontal direction.

Combining equations 21 and 23 with equation 9 yield the transformed matrix differential equation

$$\partial_3 \tilde{\mathbf{w}} = i\omega \begin{bmatrix} -p_3 & 0 \\ 0 & p_3 \end{bmatrix} \tilde{\mathbf{w}} - \gamma(x_3) \begin{bmatrix} 0 & 1 \\ 1 & 0 \end{bmatrix} \tilde{\mathbf{w}}. \quad (24)$$

Comparing the flux-normalized system of equations in equation 24 with the conventional pressure-normalized system of equations in equation 15, we see that in equation 24 only the off-diagonal terms (depending on the reflectivity function $\gamma(x_3)$) are present. Further, by neglecting interaction between the flux-normalized directional decomposed components, the flux-normalized matrix differential equation becomes independent of the reflectivity function $\gamma(x_3)$. Finally, we note that

$$\begin{aligned} \tilde{\mathbf{w}}(\omega, k_1, k_2, x_3) &= \sqrt{\frac{2}{Z}} \mathbf{w}(\omega, k_1, k_2, x_3) \\ &= \sqrt{\frac{2k_3}{\rho\omega}} \mathbf{w}(\omega, k_1, k_2, x_3). \end{aligned} \quad (25)$$

At an interface between two smoothly varying media we have $\tilde{\mathbf{w}}_+ = \tilde{L}_+^{-1} \tilde{L}_- \tilde{\mathbf{w}}_-$ with

$$\tilde{L}_+^{-1} \tilde{L}_- = \begin{bmatrix} \tilde{T}_u^{-1} & R_u \tilde{T}_u^{-1} \\ R_u \tilde{T}_u^{-1} & \tilde{T}_u^{-1} \end{bmatrix} \quad (26)$$

Here,

$$\tilde{T}_u^{-1} = \sqrt{\frac{Z_-}{Z_+}} T_u^{-1} = \frac{Z_+ + Z_-}{2\sqrt{Z_+ Z_-}} = \frac{1}{2} \left\{ \sqrt{\frac{Z_+}{Z_-}} + \sqrt{\frac{Z_-}{Z_+}} \right\}, \quad (27)$$

where Z_- denotes the impedance at the bottom of the previous thin layer and Z_+ denotes the impedance at the top of the next layer.

Zhang et al. (2005) in their equations 27 and 28 use the scaling $\tilde{\mathbf{w}} = \sqrt{k_3} \mathbf{w}$ so they are not using flux-normalized variables. With their scaling, the transformed matrix differential equation will only be of the form of equation 24 for a medium with constant density.

ONE-WAY WAVE-EQUATIONS

We shall obtain one-way equations for the up- and down-going waves by neglecting the interaction terms in equations 15 and 20. This gives the zero-order WKB approximation (Clayton and Stolt, 1981; Ursin, 1984) obeying the equations

$$\frac{\partial}{\partial x_3} \begin{bmatrix} U \\ D \end{bmatrix} = \begin{bmatrix} -ik_3 + \gamma & 0 \\ 0 & ik_3 + \gamma \end{bmatrix} \begin{bmatrix} U \\ D \end{bmatrix} \quad (28)$$

with interface conditions

$$\begin{bmatrix} U \\ D \end{bmatrix}_+ = T_u^{-1} \begin{bmatrix} U \\ D \end{bmatrix}_-. \quad (29)$$

In a region with smoothly varying parameters, the equation

$$\frac{\partial D}{\partial x_3} = (ik_3 + \gamma) D \quad (30)$$

with $D(x_3^0)$ given, has the solution

$$\begin{aligned} D(x_3) &= D(x_3^0) \exp \left[\int_{x_3^0}^{x_3} (ik_3(\zeta) + \gamma(\zeta)) d\zeta \right] \\ &= D(x_3^0) \sqrt{\frac{Z(x_3)}{Z(x_3^0)}} \exp \left[\int_{x_3^0}^{x_3} (ik_3(\zeta)) d\zeta \right]. \end{aligned} \quad (31)$$

The solution to equations 28 and 29 in the zero-order WKB approximation becomes

$$D(x_3) = D(x_3^0) T(x_3) \exp \left[i \int_{x_3^0}^{x_3} k_3(\zeta) d\zeta \right] \quad (32)$$

and

$$U(x_3) = U(x_3^0) T(x_3) \exp \left[-i \int_{x_3^0}^{x_3} k_3(\zeta) d\zeta \right]. \quad (33)$$

The factor

$$\begin{aligned} T(x_3) &= \sqrt{\frac{Z(x_3)}{Z(x_3^0)}} \prod_{0 < x_{3k} < x_3} T_u^{-1}(x_{3k}) \sqrt{\frac{Z(x_{3k-})}{Z(x_{3k+})}} \\ &= \sqrt{\frac{Z(x_3)}{Z(x_3^0)}} \prod_{0 < x_{3k} < x_3} \tilde{T}_u^{-1}(x_{3k}) \end{aligned} \quad (34)$$

is due to the interfaces between the inhomogeneous layers.

For the flux-normalized up- and downgoing waves we obtain from equations 32 to 34 using equation 25:

$$\tilde{D}(x_3) = \tilde{D}(x_{30}) \prod_{0 < x_{3k} < x_3} \tilde{T}_u^{-1}(x_{3k}) \exp \left[\int_{x_3^0}^{x_3} ik_3(\zeta) d\zeta \right] \quad (35)$$

and

$$\tilde{U}(x_3) = \tilde{U}(x_3^0) \prod_{0 < x_{3k} < x_3} \tilde{T}_u^{-1}(x_{3k}) \exp \left[- \int_{x_3^0}^{x_3} ik_3(\zeta) d\zeta \right]. \quad (36)$$

These equations could, of course, also have been obtained directly by neglecting the interaction terms in equation 24 and 26.

IMAGING CONDITIONS

In order to investigate the amplitude versus angle (AVA) or amplitude versus slowness (AVP) behavior of imaging with the different wavefield separation methods, we shall consider the simple case of a point source at a distance x_3 above a plane reflector. See Figure 1.

The initial downgoing wavefield is

$$D_0 = D(\omega, k_1, k_2, x_3 = 0) = -\frac{2\pi S(\omega)}{i\omega k_3}. \quad (37)$$

The inverse Fourier transform of equation 37 with respect to k_1 and k_2 is known as the Weyl integral (Aki and Richards, 1980). $S(\omega)$ is the Fourier transform of the effective source signature. The reflected wavefield is recorded at the same level as the source, and it is given by (suppressing the function arguments)

$$\begin{aligned} U_0 &= U(\omega, k_1, k_2, x_3 = 0) \\ &= D_0 \exp [ik_3 x_3] R(p_1, p_2) \exp [ik_3 x_3], \end{aligned} \quad (38)$$

where $R(p_1, p_2)$ is the reflection coefficient at depth x_3 . It depends only on the horizontal slowness (see Appendix)

$$p = \sqrt{p_1^2 + p_2^2}. \quad (39)$$

With amplitude-normalized separation of the up- and downgoing wavefields, wavefield extrapolation gives, at depth x_3 ,

$$\begin{aligned} D &= D_0 \exp [ik_3 x_3] \\ U &= U_0 \exp [-ik_3 x_3]. \end{aligned} \quad (40)$$

Imaging, or estimation of the reflection coefficient, is performed by cross-correlation in the wavenumber domain at depth x_3 . This gives for amplitude-normalized variables

$$\begin{aligned} I_A(p_1, p_2) &= \int U D^* d\omega \\ &= R(p_1, p_2) \int |D_0|^2 d\omega \\ &= R(p_1, p_2) \frac{F(\omega)}{p_3^2}, \end{aligned} \quad (41)$$

where

$$F(\omega) = \left| \frac{2\pi S(\omega)}{\omega} \right|^2. \quad (42)$$

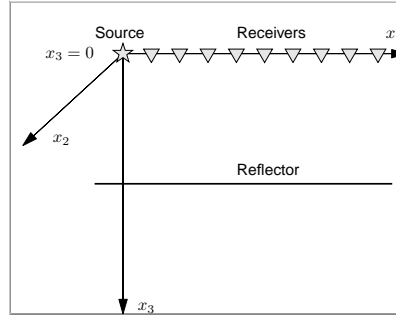


Figure 1: Simple geometry for imaging conditions.

For flux-normalized variables, $\tilde{\mathbf{w}} = \sqrt{\frac{2p_3}{\rho}} \mathbf{w}$ we obtain

$$\begin{aligned} I_F(p_1, p_2) &= \int \tilde{U} \tilde{D}^* d\omega \\ &= R(p_1, p_2) \int |\tilde{D}_0|^2 d\omega \\ &= R(p_1, p_2) \frac{2F(\omega)}{\rho p_3}. \end{aligned} \quad (43)$$

Sun and Zhang (2009) have proposed a migration scheme where the initial conditions for the downward continued wavefield is

$$\bar{D}_0 = -\frac{S(\omega)}{i\omega}. \quad (44)$$

This gives the cross-correlation image

$$\begin{aligned} I_Z(p_1, p_2) &= \int U \bar{D}_0^* d\omega \\ &= R(p_1, p_2) \int D_0 \bar{D}_0^* d\omega \\ &= R(p_1, p_2) \frac{F(\omega)}{2\pi p_3}. \end{aligned} \quad (45)$$

Since $p_3 = \cos(\theta)/c$ it is seen that the first cross-correlation in equation 41 is divided by $\cos^2(\theta)$, while the two last in equations 43 and 45 only are divided by $\cos(\theta)$. It is customary to estimate the AVA response by multiplying an AVA response obtained from a cross-correlation image condition with $\cos(\theta)$. Then only the two last cross-correlations will give correct AVA behavior. This confirms what previously has been found by Zhang et al. (2005) and Sun and Zhang (2009). Multiplying the cross-correlation AVA response with $\cos(\theta)$ gives incorrect result for the amplitude-normalized wavefields, but the one of new initial data give correct result.

We note that in this simple example, the two first methods give correct result by computing

$$\begin{aligned} R(p_1, p_2) &= \frac{\int U D^* d\omega}{\int |D_0|^2 d\omega} \\ &= \frac{\int \tilde{U} \tilde{D}^* d\omega}{\int |\tilde{D}_0|^2 d\omega}. \end{aligned} \quad (46)$$

In the last method, some care must be used since

$$R(p_1, p_2) = \frac{\int U \bar{D}^* d\omega}{\int D_0 \bar{D}_0^* d\omega}. \quad (47)$$

HETEROGENEOUS MEDIUM

We want to use one-way wave propagators for migration in a heterogeneous medium. Based on the previous discussion we choose to use flux-normalized variables. The downgoing field from a point source is then represented in the wavenumber-frequency domain by

$$\tilde{D}_0(\omega, k_1, k_2, 0) = 2\pi i \sqrt{\frac{2}{\rho \omega k_3}} S(\omega). \quad (48)$$

In marine seismic data we may add the effect of the free surface (the ghost) on the downgoing wavefield (Amundsen and Ursin, 1991):

$$\begin{aligned} \tilde{D}_0(\omega, k_1, k_2, 0) &= 2\pi i \sqrt{\frac{2}{\rho \omega k_3}} \\ &\times (\exp[-ik_3 x_3^s] - R_0 \exp[ik_3 x_3^s]) S(\omega), \end{aligned} \quad (49)$$

where x_3^s is the source depth, and the reflection coefficient is theoretically $R_0 = 1$.

If the wavefield is acquired by a conventional streamer configuration, only pressure is recorded. The primary upgoing wavefield U can then be estimated by a demultiple procedure (Robertsson and Kragh, 2002; Amundsen, 2001), where ghost and free-surface multiples are removed from the data. Hence, using equation 25 the flux-normalized upgoing wavefield can be represented by

$$\tilde{U}_0 = \sqrt{\frac{2}{Z}} U_0. \quad (50)$$

The pressure and the vertical displacement velocity can be measured in ocean-bottom seismic acquisition. Recent development (Tenghamn et al., 2008; Landrø and Amundsen, 2007) also allows for both these to be measured on a streamer configuration. Then the flux-normalized upgoing wavefield is given by

$$\tilde{U}_0 = \frac{1}{\sqrt{2Z}} [P - ZV_3]. \quad (51)$$

The downward continuation of the wavefields is done by solving the equation

$$\frac{\partial \tilde{\mathbf{w}}}{\partial x_3} = \begin{bmatrix} -i\hat{H}_1 & 0 \\ 0 & i\hat{H}_1 \end{bmatrix} \tilde{\mathbf{w}} \quad (52)$$

for $x_3 > 0$ with $\tilde{\mathbf{w}}(0) = [\tilde{U}_0, \tilde{D}_0]^T$ given in equation 49 - 51. Equation 52 is a generalization of equation 24 with the coupling terms neglected. The operator \hat{H}_1 is the square-root operator satisfying (Wapenaar, 1998)

$$\hat{H}_1 \hat{H}_1 = \left(\frac{\omega}{c}\right)^2 + \rho \frac{\partial}{\partial x_1} \left(\frac{1}{\rho} \frac{\partial}{\partial x_1} \cdot\right) + \rho \frac{\partial}{\partial x_2} \left(\frac{1}{\rho} \frac{\partial}{\partial x_2} \cdot\right). \quad (53)$$

By dividing the medium into thin slabs of thickness Δx_3 with negligible variations in the preferred direction x_3 of propagation within each slab, allows us to extend the propagator to a general inhomogeneous medium with small lateral medium variations using for example split-step (Stoffa et al., 1990), Fourier finite difference (Ristow and Rühl, 1994), or a phase-screen (Wu and Huang, 1992) approach depending on the size of the medium heterogeneities in the lateral direction (Zhang et al., 2009).

At thin-slab boundaries one may apply a correction term for the transmission loss (see Appendix):

$$\tilde{T}_u^{-1} = \frac{1}{2} \left[\sqrt{\frac{Z_+}{Z_-}} + \sqrt{\frac{Z_-}{Z_+}} \right]. \quad (54)$$

Cao and Wu (2006) have proposed a similar correction for the downward continuation of pressure.

The downward continued wavefields can be used in a standard way to create an image. One may also apply a cross-correlation and a local Fourier transform to compute common-angle gathers (de Bruin et al., 1990; Sava and Fomel, 2003; de Hoop et al., 2006; Sun and Zhang, 2009). This is termed the wave-equation angle transform, and a common-image gather for a single shot is

$$I(\mathbf{x}, \mathbf{p}) = \frac{1}{2\pi} \iint U\left(\mathbf{x} + \frac{\mathbf{h}}{2}, \omega\right) D^*\left(\mathbf{x} - \frac{\mathbf{h}}{2}, \omega\right) e^{-i\omega \mathbf{p} \cdot \mathbf{h}} d\mathbf{h} d\omega, \quad (55)$$

where $\mathbf{h} = (h_1, h_2, 0)$ is the horizontal offset coordinate and $\mathbf{p} \cdot \mathbf{h} = p_1 h_1 + p_2 h_2$. In Appendix it is shown that this approach produces an estimate of the plane-wave reflection coefficient multiplied by the energy of the corresponding downgoing plane wave. In order to obtain an unbiased estimate of the reflection coefficient it is necessary to divide by this factor (which we will refer to as the *source correction term*), exactly as in equation 46. This gives the estimate

$$R_{AT}(\mathbf{x}, \mathbf{p}) = \frac{1}{2\pi} \frac{\iint U\left(\mathbf{x} + \frac{\mathbf{h}}{2}, \omega\right) D^*\left(\mathbf{x} - \frac{\mathbf{h}}{2}, \omega\right) e^{-i\omega \mathbf{p} \cdot \mathbf{h}} d\mathbf{h} d\omega}{\int |\hat{D}(\mathbf{x}, \omega \mathbf{p}, \omega)|^2 d\omega}. \quad (56)$$

It may be necessary to apply a stabilizing procedure as discussed in Vivas et al. (2009). In order to obtain an estimate of the reflection coefficient for a range of p -values it is necessary to average the expression in equation 56 over many shots.

NUMERICAL RESULTS

Throughout our numerical examples, we employ a Fourier finite-difference approach to account for lateral medium variations. Further, we consider wave-propagation in a 2D medium.

First we extract amplitude information after migration using flux-normalized wavefields in a lateral invariant medium. The input data to migration is modelled over a medium with density contrasts only; hence, the reflection coefficients are independent of angle. Next, we compare conventional pressure normalization to the flux-normalized approach on a field data example where we in a quantitative fashion compare the estimated reflectivity. For the flux-normalized approach we use equations 35 and 36 combined with equation B-2 for the wave propagation. For the pressure-normalized approach, we use equations 32 and 33 and set the transmission correction to unity. Equation 56 is used to output AVP gathers on selected locations.

Imaging in a lateral invariant medium

In our first test, we consider a laterally invariant medium with a constant velocity of 2000 m/s and with density contrasts in depth at 1, 2, and 3 km as illustrated in Figure 2. We choose this model since in this particular case we will have angle independent reflection coefficients. We create a synthetic split-spread shot-gather over the laterally invariant medium using a finite-difference modelling scheme. In Figure 3 we show the modelled shot, and the migrated shot is shown in Figure 4.

To extract AVP or AVA information at a reflector position, we need information from more than one shot since each shot gives limited angle information. A schematic representation of angle information available from one shot is shown in Figure 5. Using information from the wave-equation angle-transform, this can further be illustrated by plotting $I(\mathbf{x}, p)$ (in gray-scale) overlaid the source correction term (in color-scale) at midpoints $x_{m,1} = -0.5$ km, $x_{m,2} = 0.0$ km, and $x_{m,3} = 0.5$ km shown in Figure 6.

By simulating more shots over one midpoint location x_m , we can extract angle information for larger angle coverage as shown schematically in Figure 7. We simulate 100 shots with a shot-distance of 10 m on both sides of x_m , in addition to one shot just above x_m . This produces the angle coverage shown in Figure 8, where we plot $I(\mathbf{x}, p)$ overlaid the corresponding source illumination for the fixed midpoint location x_m . We notice that the angle coverage for each reflector in depth is different (as expected).

At each reflector depth, we extract the peak amplitude of $R_{AT}(x_m, \theta)$ using equation 56. The result is depicted in Figure 9. We have plotted the AVA response for the reflector at 1 km up to 50 degrees (in red), the reflector at 2 km up to 35 degrees (in green) and the reflector at 3 km up to 25 degrees (in blue). In this example, we expect an angle-independent reflectivity, and from the result we see

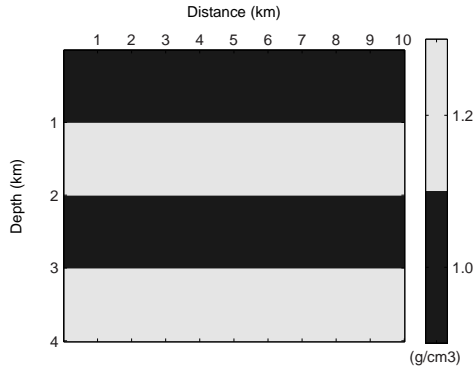


Figure 2: Densities used in the finite-difference modelling over the lateral invariant model example.

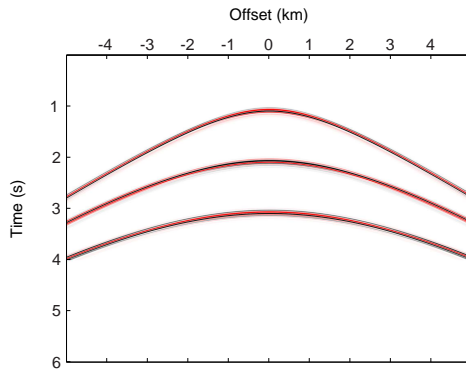


Figure 3: A synthetic shot-gather from a finite-difference modelling over the lateral invariant model example.

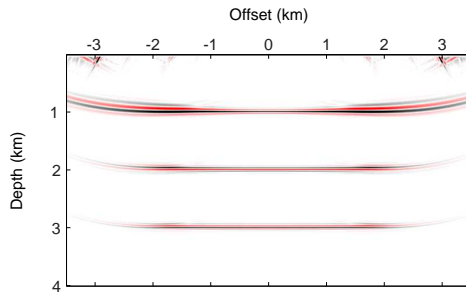


Figure 4: Migrated shot from the lateral invariant model with flux-normalized wavefields.

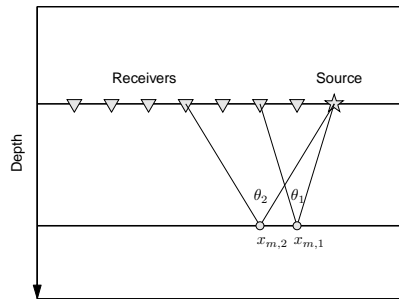


Figure 5: Schematic representation of angle information contained in one shot, where $x_{m,1}$ and $x_{m,2}$ are midpoint locations with information around angles θ_1 and θ_2 . For each midpoint location, each shot only gives limited angle information.

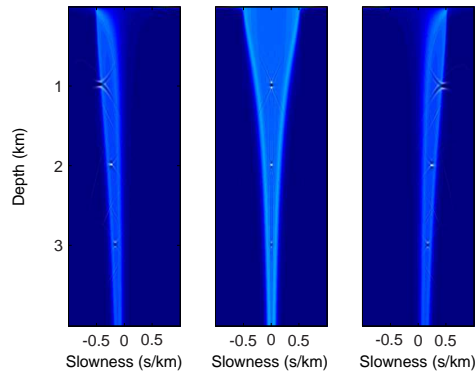


Figure 6: Slowness coverage $I(\mathbf{x}, p)$ from one shot (gray-scale) overlaid the corresponding source correction (color-scale) for (left) $x_{m,1} = -0.5$ km; (middle) $x_{m,2} = 0.0$ km; and (right) $x_{m,3} = 0.5$ km.

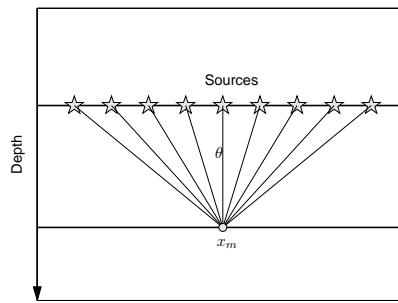


Figure 7: Schematic representation of angle coverage θ at one midpoint location x_m from a range of shots. To extract a larger range of angle coverage, each midpoint location requires several shots.

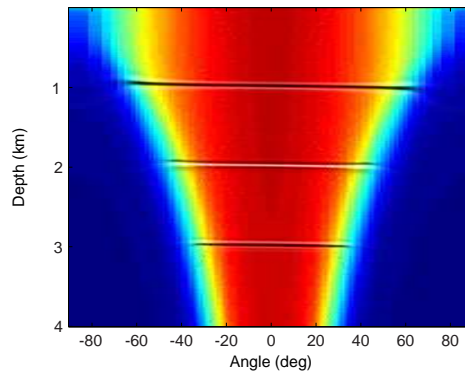


Figure 8: Angle coverage $I(\mathbf{x}, p)$ (gray-scale) from one spatial location x_m overlaid the corresponding source correction (color-scale) where the contribution from multiple shots are included.

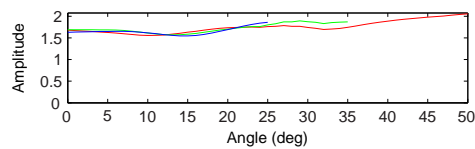


Figure 9: Peak amplitudes at each reflector at 1 km (red), 2 km (green), and 3 km (blue) for one spatial location x_m .

that the reflectivity is recovered relatively accurately for a wide range of angles. Due to a limited aperture, edge effects impact the results, and the largest angles on each reflector are affected.

Marine field seismic data example

We apply both conventional pressure-normalized and the derived flux-normalized methods to a field dataset from the Nordkapp Basin. The basin is located offshore Finnmark, in the Norwegian sector of the Barents Sea. It is an exploration area which exhibits complex geology and is challenging for seismic imaging. We have extracted a subset of a 2D survey which covers two salt dome structures partially. In Figure 10, the velocity model used in the migration is shown.

The dataset is composed by collecting and combining streamer data in two directions, providing a split-spread configuration. Each shot is separated by 25.0 m, and in our example we have included a total of 775 shots. Each streamer has 1296 receivers with a hydrophone distance of 12.5 m and a total offset of about 8100 m on both sides of the source location. Notice that no demultiple is applied in the pre-processing step. In Figure 11 we show one extracted shot which is input to migration.

In the imaging, we have used a source signature comparable to a Ricker wavelet with a peak frequency of 17 Hz. We used 3-35 Hz of the frequency content of the data, and imaged the data down to 10 km. The total aperture of each shot was 16 km. For both the pressure-normalized and the flux-normalized wavefield decomposition, we migrate the dataset with the same downward continuation scheme and the same imaging condition. That is, we use a third-order Fourier finite-difference migration operator and an image condition which estimates the reflectivity by accounting for the source illumination. The flux-normalized migration has an approximation to the transmission loss correction applied at thin-slab boundaries using the minimum velocity at each slab given by the aperture of each migrated shot. In Figures 12 and 13 the pressure-normalized and the flux-normalized migrated sections are shown, respectively. By inspecting and comparing both sections, we see that we have an apparent similar amplitude response.

To quantify the difference between the migrated sections, we compute the difference between the absolute value of each section. The difference plot is shown in Figure 14. The red and black colors indicate that the flux-normalized image provides higher and lower amplitudes than the pressure-normalized image, respectively. In the shallower part of the difference image, from the surface to about 2 km, the pressure-normalized image appears to be dominating; however, these parts of the sections are also contaminated by low frequent migration noise. In the sediment basin between the two salt-domes, that is, below and around a distance of 6 km, no coherent energy appears below 2 km. Around approximately a distance of

14 km to 16 km at around depth 8 km, the flux-normalized images gives a higher amplitude response on some parts of a few subsurface reflectors. The peak amplitude difference is around one-tenth of the reflectivity image amplitudes.

Further, we extract a slowness gather from each of the migration approaches corresponding to lateral position of 14.4 km and these are shown in Figure 15. Figure 15(a) and Figure 15(b) shows the output from the pressure-normalized and flux-normalized approach, respectively. The gathers looks similar. Next, we extract one event at 7.8 km of depth on these gathers, as shown in Figure 16. For this event we extract the peak amplitudes for each of the migrated reflectors, and plot these in Figure 17 (top), where the red curve is the flux-normalized and the blue curve is the pressure normalized peak amplitudes. Finally, we take the difference between the normalized peak amplitudes (bottom), where the positive and negative values correspond to higher and lower peak amplitudes when using flux-normalized variables. The plot shows differences between the results from the different approaches, and explains the difference plot in Figure 14.

CONCLUSIONS

By directional decomposing a wavefield using a flux-normalized eigenvalue decomposition, we have derived initial conditions for pre-stack depth migration of common-shot data. This decomposition simplifies the system of differential equations. Further, by neglecting interaction between directional components, we derive propagators for flux-normalized wavefields where we formulate a transmission loss compensation approach for flux-normalized wavefield propagation. By using the wave-equation angle transform, we formulate an unbiased estimate of the reflection coefficient. From our one-dimensional numerical example, we show that a flux-normalized directional decomposition provides accurate amplitude information in a medium where the parameters are function of depth only. Finally, we extend our approach to a laterally varying media. From a field data example, we observe some differences in the strength of the estimated reflectivity compared to a pressure-normalized approach.

ACKNOWLEDGMENTS

The authors would like to thank Hans-Kristian Helgesen and Robert Ferguson for useful discussions, and Statoil for permission to publish data from the Nordkapp basin. This research has received financial support from the Norwegian Research Council via the ROSE project. Bjørn Ursin has also received financial support from VISTA.

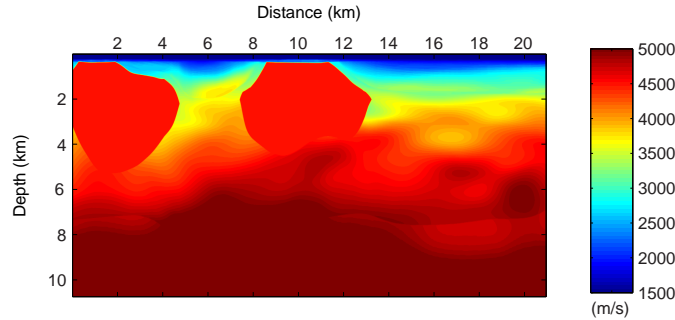


Figure 10: The velocity model used in the Nordkapp field data example.

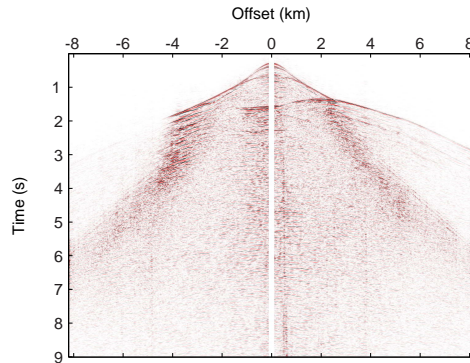


Figure 11: One extracted shot-gather used in the Nordkapp basin field data example.

APPENDIX A

THE WAVE-EQUATION ANGLE TRANSFORMS

In terms of local Fourier transforms, the common-image gather in equation 55 can be expressed by

$$I(\mathbf{x}, \mathbf{p}) = \left(\frac{1}{2\pi}\right)^5 \iiint \hat{U}(\mathbf{x}, \mathbf{k}^r, \omega) \hat{D}^*(\mathbf{x}, \mathbf{k}^s, \omega) e^{i\mathbf{k}^r \cdot \mathbf{h}/2} e^{i\mathbf{k}^s \cdot \mathbf{h}/2} e^{-i\mathbf{p} \cdot \mathbf{h}} d\mathbf{k}^r d\mathbf{k}^s d\omega \quad (\text{A-1})$$

where $\mathbf{k}^r = (k_1^r, k_2^r)$ and $\mathbf{k}^s = (k_1^s, k_2^s)$. Snell's law is

$$\hat{U}(\mathbf{x}, \mathbf{k}^r, \omega) = R(\mathbf{x}, \mathbf{q}) \hat{D}^*(\mathbf{x}, \mathbf{k}^s, \omega) (2\pi)^2 \delta(\mathbf{k}^r - \mathbf{k}^s). \quad (\text{A-2})$$

Inserted in equation A-1 this gives

$$I(\mathbf{x}, \mathbf{p}) = \left(\frac{1}{2\pi}\right)^3 \iiint R(\mathbf{x}, \mathbf{q}) |\hat{D}(\mathbf{x}, \mathbf{k}, \omega)|^2 e^{i(\mathbf{k} - \omega\mathbf{p}) \cdot \mathbf{h}} d\mathbf{k} d\omega \quad (\text{A-3})$$

where $\mathbf{k}^r = \mathbf{k}^s = \mathbf{k} = \omega\mathbf{p}$. Further simplifications gives

$$\begin{aligned} I(\mathbf{x}, \mathbf{p}) &= \frac{1}{2\pi} \iint R(\mathbf{x}, \mathbf{q}) |\hat{D}(\mathbf{x}, \mathbf{k}, \omega)|^2 \delta(\mathbf{k} - \omega\mathbf{p}) d\mathbf{k} d\omega \\ &= R(\mathbf{x}, \mathbf{q}) \int |\hat{D}(\mathbf{x}, \mathbf{k}, \omega)|^2 d\omega \end{aligned} \quad (\text{A-4})$$

The derivations above are only approximate, since finite-aperture effects have not been taken into consideration.

APPENDIX B

APPROXIMATE TRANSMISSION AND REFLECTION COEFFICIENTS

The correction factor for downward propagation of the up- and downgoing wavefields is the transmission coefficient in equation 27:

$$\tilde{T}_u^{-1} = T_u^{-1} \left(\frac{Z_-}{Z_+} \right) = \frac{Z_+ + Z_-}{2\sqrt{Z_- Z_+}}. \quad (\text{B-1})$$

With $Z_- = Z$ and $Z_+ = Z + \Delta$ this becomes

$$\begin{aligned} \tilde{T}_u^{-1} &= \frac{2Z + \Delta}{2\sqrt{Z(Z + \Delta)}} \\ &= \frac{2Z + \Delta}{2Z\sqrt{1 + \frac{\Delta}{Z}}} \\ &\approx \frac{2Z + \Delta}{2Z\left(1 + \frac{\Delta}{2Z} - \frac{1}{8}\left(\frac{\Delta}{Z}\right)^2\right)} \\ &= \frac{2Z + \Delta}{2Z + \Delta - \frac{Z\Delta}{4Z}} \\ &\approx 1 + \frac{1}{8}\left(\frac{\Delta}{Z}\right)^2 \end{aligned} \quad (\text{B-2})$$

Using equation 12 for Z we obtain

$$\frac{\Delta}{Z} = \frac{\Delta(\rho c)}{\rho c} + \tan(\theta)\Delta\theta. \quad (\text{B-3})$$

With

$$\sin(\theta) = pc \quad (\text{B-4})$$

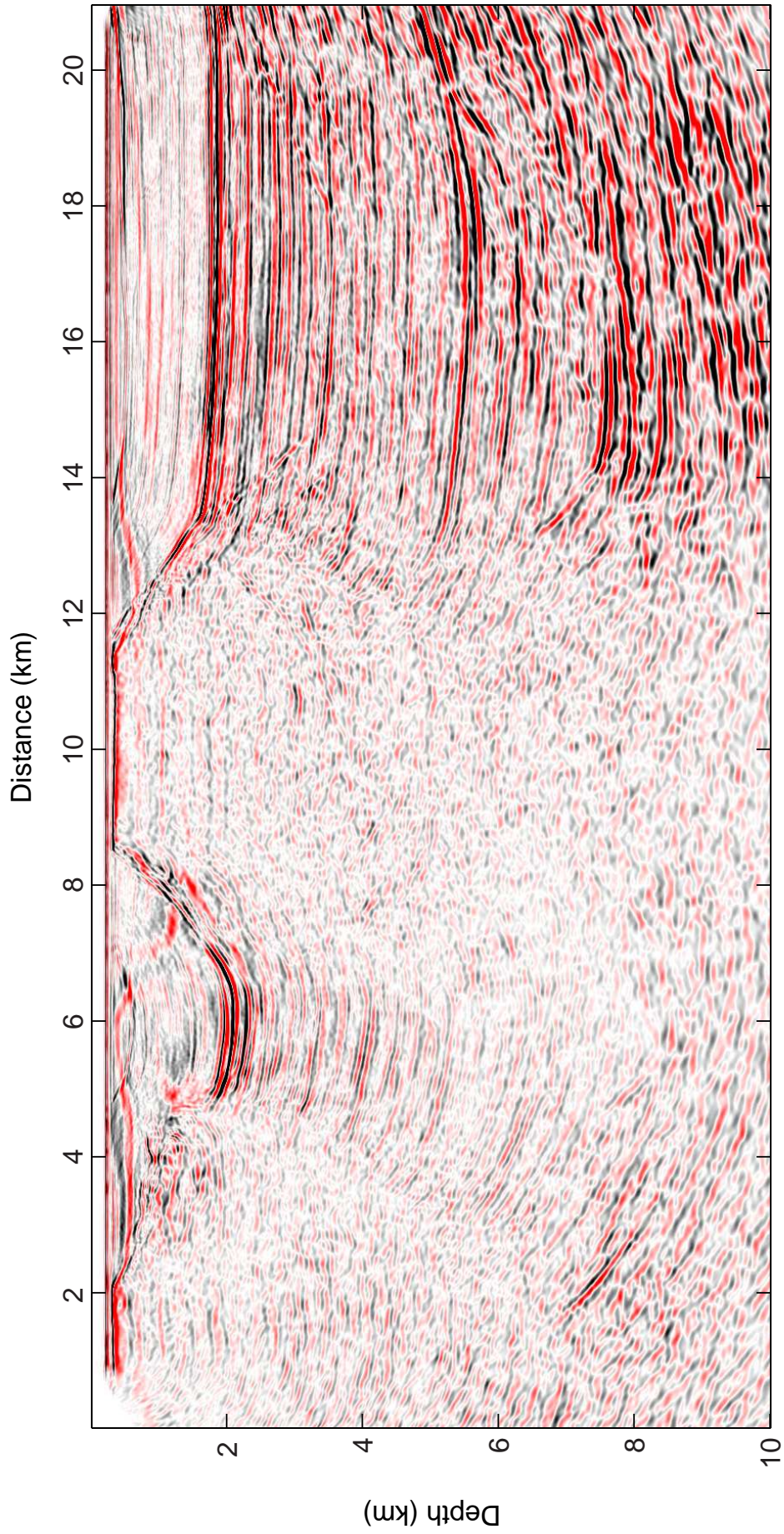


Figure 12: Migrated image of the Nordkapp field example with the pressure-normalized wavefield decomposition and migration approach.

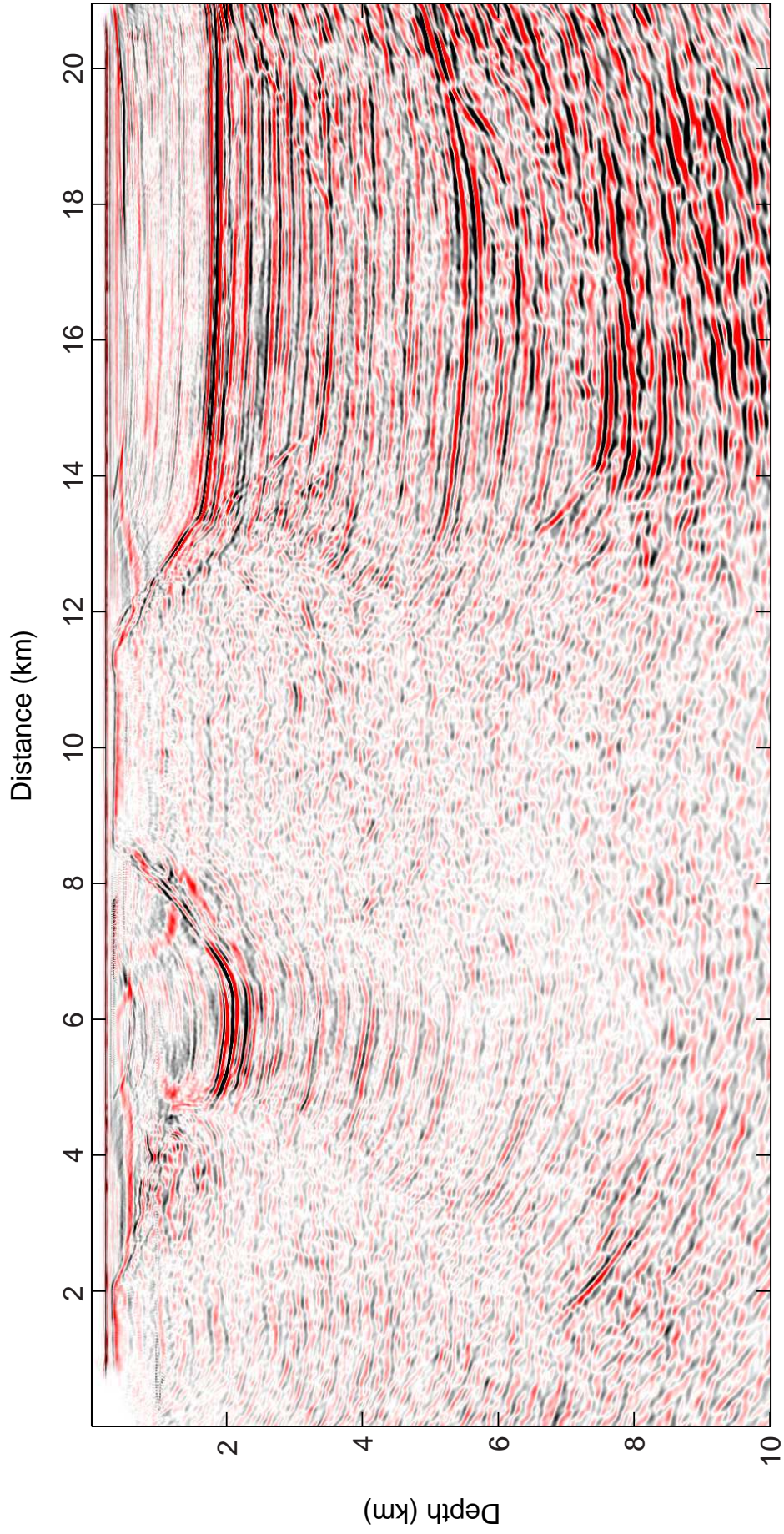


Figure 13: Migrated image of the Nordkapp field example with the flux-normalized wavefield decomposition and migration approach.

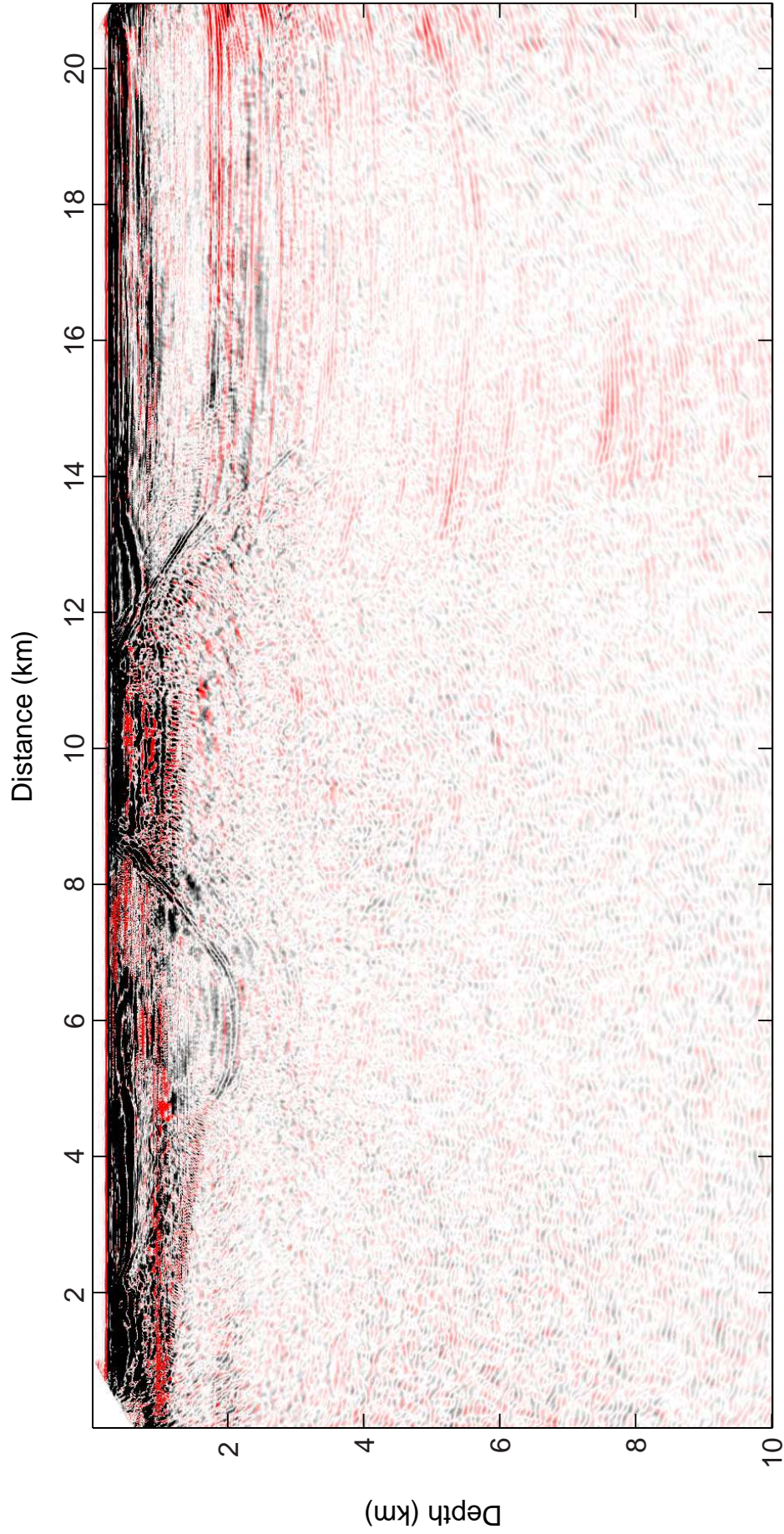


Figure 14: Difference of the absolute value of the migrated flux-normalized wavefield decomposition and the pressure-normalized wavefield decomposition sections of the Nordkapp field example. The red color indicates that the flux-normalized image is dominating, and black color indicates that the pressure-normalized image is dominating.

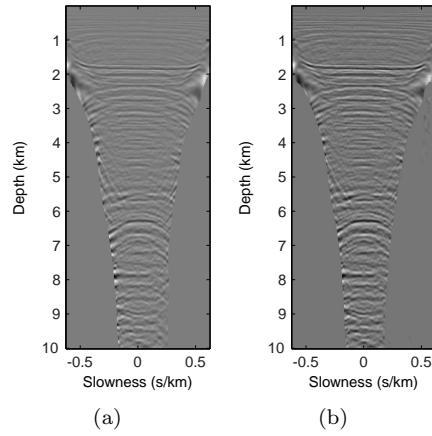


Figure 15: Slowness-gather at a distance of 14.4 km from the Nordkapp basin field data example. (a) with pressure-normalized and (b) flux-normalized variables.

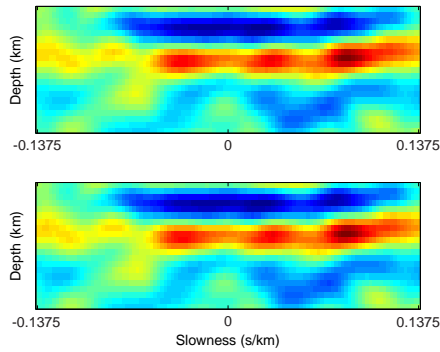


Figure 16: Extracted event at 7.8 km depth from the slowness-gathers in Figure 15 at a distance of 14.4 km for (top) flux-normalized variables and (bottom) pressure-normalized variables.

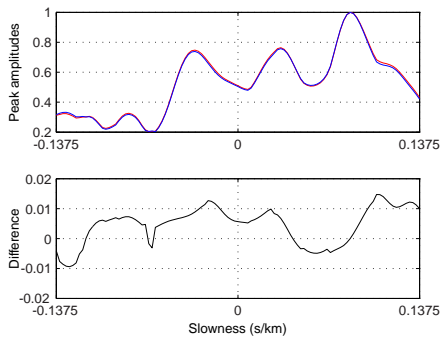


Figure 17: Normalized peak amplitudes along event in 16 (top) with flux-normalized variables (red line) and pressure-normalized variables (blue line). Difference between normalized peak amplitudes (bottom), where positive and negative values corresponds to higher and lower peak amplitudes in using flux-normalized variables.

(p as in horizontal slowness in equation 39)

$$\Delta(\theta) = \tan(\theta) \frac{\Delta c}{c} \quad (\text{B-5})$$

so that

$$\frac{\Delta}{Z} = \frac{\Delta(\rho c)}{\rho c} + \tan^2(\theta) \frac{\Delta c}{c}. \quad (\text{B-6})$$

The reflection coefficient is approximated by

$$R_d = \frac{Z_+ - Z_-}{Z_+ + Z_-} \approx \frac{\Delta}{2Z}. \quad (\text{B-7})$$

The correction term in equation B-2 is second order in the change in impedance, and it is normally small. However, in the computation of the one-way wavefields there appears a product of such terms. This may not be small, and it should therefore be corrected for.

REFERENCES

- Aki, K. and P. G. Richards, 1980, Quantitative seismology, theory and methods: Volume 1: W. H. Freeman and Company.
- Amundsen, L., 2001, Elimination of free-surface related multiples without need of the source wavelet: *Geophysics*, **66**, 327–341.
- Amundsen, L. and B. Ursin, 1991, Frequency-wavenumber inversion of acoustic data: *Geophysics*, **56**, 1027–1039.
- Bremmer, H., 1951, The W.K.B. approximation as the first term of a geometric-optical series: *Communications on Pure and Applied Mathematics*, **4**, 105–115.
- Cao, J. and R.-S. Wu, 2006, Study of the influence of propagator amplitude correction on image amplitude using beamlet propagator with local WKBJ approximation: SEG Technical Program Expanded Abstracts, **25**, 2499–2503.
- , 2008, Amplitude compensation for one-way wave propagators in in homogeneous media and its application to seismic imaging: *Commun. Comput. Phys.*, **3**, 203–221.
- Claerbout, J., 1976, Fundamentals of geophysical data processing: McGraw-Hill New York.
- Claerbout, J. F., 1970, Coarse grid calculations of waves in inhomogeneous media with application to delineation of complicated seismic structure: *Geophysics*, **35**, 407–418.
- , 1971, Toward a unified theory of reflector mapping: *Geophysics*, **36**, 467–481.
- Clayton, R. W. and R. H. Stolt, 1981, A Born-WKBJ inversion method for acoustic reflection data: *Geophysics*, **46**, 1559–1567.
- de Bruin, C. G. M., C. P. A. Wapenaar, and A. J. Berkhout, 1990, Angle-dependent reflectivity by means of prestack migration: *Geophysics*, **55**, 1223–1234.
- de Hoop, M., R. van der Hilst, and P. Shen, 2006, Wave-equation reflection tomography: annihilators and sensitivity kernels: *Geophysical Journal International*, **167**, 1332–1352.
- Kiyashchenko, D., R.-E. Plessix, B. Kashtan, and V. Troyan, 2005, Improved amplitude multi-one-way modeling method: *Wave Motion*, **43**, 99–115.
- Landrø, M. and L. Amundsen, 2007, Fighting the ghost: *Geo ExPro*, 78–80.
- Pierce, A. D., 1981, Acoustics: An introduction to its physical principles and applications: McGraw-Hill.
- Ristow, D. and T. Rühl, 1994, Fourier finite-difference migration: *Geophysics*, **59**, 1882.
- Robertsson, J. O. A. and E. Kragh, 2002, Rough-sea deghosting using a single streamer and a pressure gradient approximation: *Geophysics*, **67**, 2005–2011.
- Sava, P. and S. Fomel, 2003, Angle-domain common-image gathers by wavefield continuation methods: *Geophysics*, **68**, 1–065.
- Stoffa, P. L., J. T. Fokkema, R. M. de Luna Freire, and W. P. Kessinger, 1990, Split-step Fourier migration: *Geophysics*, **55**, 410–421.
- Sun, J. and Y. Zhang, 2009, Practical issues of reverse time migration: true amplitude gathers, noise removal and harmonic-source encoding: ASEG Extended Abstracts.
- Tenghamn, R., S. Vaage, and C. Borresen, 2008, GeoStreamer, a Dual-sensor Towed Marine Streamer: 70th EAGE Conference and Exhibition, B031.
- Ursin, B., 1983, Review of elastic and electromagnetic wave propagation in horizontally layered media: *Geophysics*, **48**, 1063–1081.
- , 1984, Seismic migration using the WKB approximation: *Geophysical Journal of the Royal Astronomical Society*, **79**, 339–352.
- , 1987, The plane-wave reflection and transmission response of a vertically inhomogeneous acoustic medium: In Bernabini, M., Carrion, P., Jacovitti, G., Rocca, F., Treitel, S., and Worthington, M., eds.: *Deconvolution and Inversion*. Blackwell Sc. Publ., Oxford, 189–207.
- van Stralen, M. J. N., M. V. de Hoop, and H. Blok, 1998, Generalized Bremmer series with rational approximation for the scattering of waves in inhomogeneous media: *The Journal of the Acoustical Society of America*, **104**, 1943–1963.
- Vivas, F. A., R. C. Pestana, and B. Ursin, 2009, A new stabilized least-squares imaging condition: *Journal of Geophysics and Engineering*, **6**, 264–268.
- Wapenaar, K., 1998, Reciprocity properties of one-way propagators: Short Note: *Geophysics, Soc. of Expl: Geophys*, **63**, 1795–1798.
- Wu, R.-S. and L.-J. Huang, 1992, Scattered field calculation in heterogeneous media using a phase-screen propagator: SEG Technical Program Expanded Abstracts, **11**, 1289–1292.
- Zhang, J., W. Wang, and Z. Yao, 2009, Comparison between the Fourier finite-difference method and the generalized-screen method: *Geophysical Prospecting*, **57**, 355–365.
- Zhang, Y., S. Xu, N. Bleistein, and G. Zhang, 2007, True-amplitude, angle-domain, common-image gathers from one-way wave-equation migrations: *Geophysics*, **72**, P49.
- Zhang, Y., G. Zhang, and N. Bleistein, 2003, True amplitude wave equation migration arising from true amplitude one-way wave equations: *Inverse Problems*, **19**, 1113–1138.
- , 2005, Theory of true-amplitude one-way wave-equations and true-amplitude common-shot migration: *Geophysics*, **72**, P49.